RESEARCH PAPER

Depletion-induced seismicity in NW-Germany: lessons from comprehensive investigations

Gerd Gudehus[1] · Christof Lempp[2] · Christian Scheffzük[4] · Birgit I. Műller[3] · Frank R. Schilling[3]

Abstract

Evaluating various investigations for north-German gas fields, we discuss past and actual evolutions of the rock fabric in the light of dilatant driven and spontaneous contractant critical phenomena. Features of the latter were discovered by multi-stage triaxial tests with water-saturated sandstone samples and were similarly observed around the gas fields. A Mohr–Coulomb condition with quasi-local stress components ($\hat{\sigma}'_1$ and $\hat{\sigma}'_3$), and variable parameters ϕ' and $\hat{c}'$, can capture successive critical states of the solid fabric. The implied driven dilatation up to a collapse with contraction is captured by a stress-dilatancy relation. Fractal patterns of shear bands (faults) dominate if the smallest principal stress $\hat{\sigma}'_3$ exceeds $\hat{c}'$, otherwise cracks dominate and can lead to a rockburst. Triaxial tests with X-ray attenuation, seismometry including the splitting of shear waves and/or neutron beam diffraction contribute to clarification and validation. Seismic early warning and calculation models for various geotechnical operations with dominating faults can thus be improved, but the task is more difficult for rockbursts.

Keywords Critical phenomena · Fractal fault patterns · Geotechnical enhancement · Neutron beam diffraction · Rockburst · Seismicity · Shear wave splitting · Triaxial tests · X-ray tomography

1 Introduction

The lion's share of the German natural gas production is achieved in Lower Saxony. In particular, gas-filled sandstone formations occur between the rivers Weser and Elbe in a depth from ca 5 km to 6 km. With a delay of almost 20 years, their depletion led to earthquakes with magnitudes of up to ca 3. Comprehensive investigations demonstrated that the depletion-induced seismicity cannot exceed the observed one (Müller et al 2020) [24]. In the present paper, we refer to these investigations and related studies.

Our objective are *critical phenomena* ($\kappa\rho\iota\sigma\iota\varsigma$=moment of decision) in a part of the Earth's crust for which a plethora of data help clarify mechanisms which prevail not only in the considered region, especially if they are *technically enhanced*. We consider the named site as a kind of rock mechanics field laboratory. Continuum approaches and materials science do not suffice due to spatial distributions of pore volume fractions and stresses with fluctuation wavelengths from the width of rock fragments to the distance of main faults. The causative critical phenomena are more intricate than thermodynamic ones, and there are multi-fractal features from small sections of the lithosphere up to the Earth's crust as a whole. Successions of them exhibit a wild randomness (Mandelbrot 1999) [20] which cannot be captured with normal distributions. This has consequences from the geological past up to geotechnical operations.

We consider first critical phenomena and their relics prior to the depletion (Sect. 2). *Tectonic* configurations ($\tau\epsilon\kappa\tau\omega\nu$ = builder or mover), states and changes of both are

✉ Gerd Gudehus
gerd.gudehus@web.de

1 Emeritus, Institute of Soil and Rock Mechanics, Karlsruhe Institute of Technology, Karlsruhe, Germany

2 Emeritus, Institute of Geosciences and Geography, University of Halle, Halle, Germany

3 Institute of Applied Geosciences, Karlsruhe Institute of Technology, Karlsruhe, Germany

4 Landeslabor Berlin-Brandenburg (formerly Institute of Applied Geosciences Karlsruhe), Institute of Technology, Karlsruhe, Germany
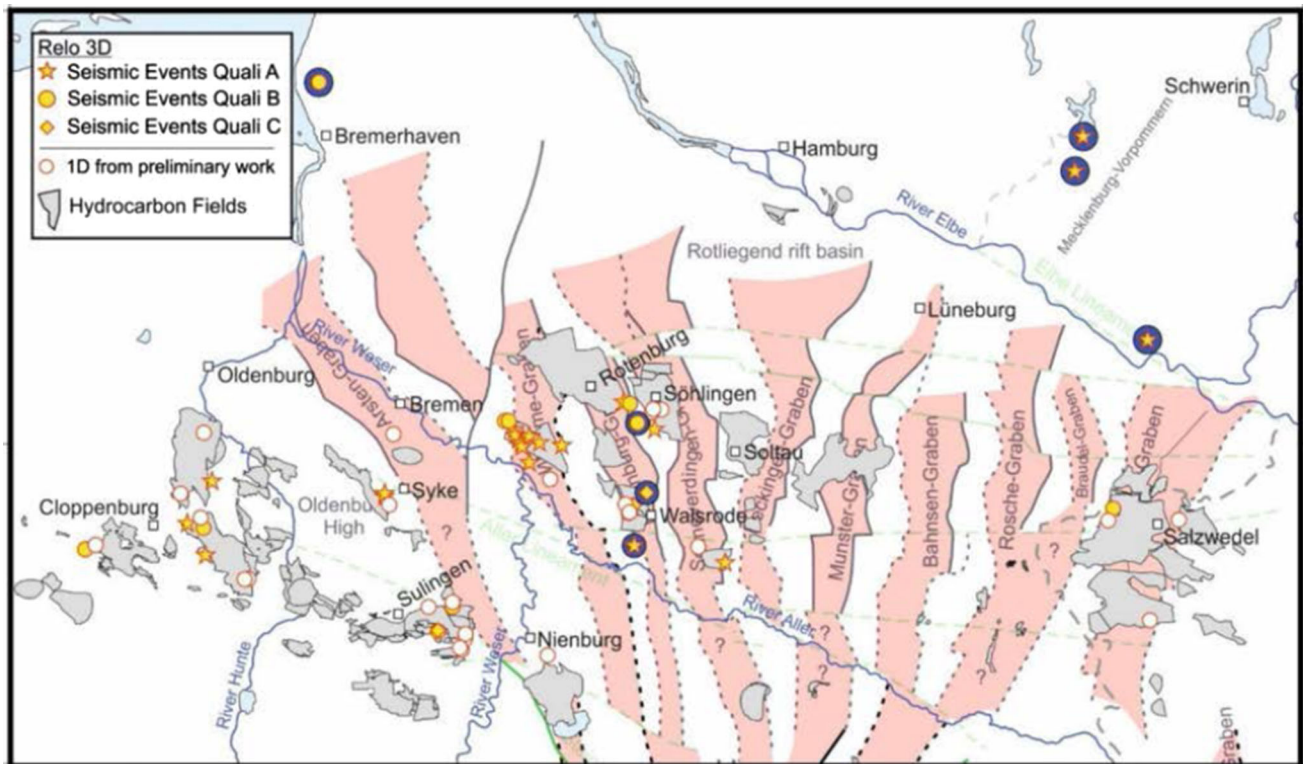
Fig. 1 Geological map for a part of Lower Saxony with tectonic structures, gas fields and seismic epicenters (located with excellent (**A**), good (**B**) and questionable (**C**) quality, blue circles for natural events), length scale as in Fig. 6 ([31], referring to [8], courtesy R Gast and P Uta)

outlined, emphasizing the inadequacy of continuum mechanics and materials science with locally confined fluctuations. The emergence of gas traps, filled with natural gas from the Carboniferous, is outlined in detail, this helps explain the regional evolution of the rock fabric with its pore system ($\pi o \rho o \varsigma$ = passage), stress and pore pressure, which is sometimes accompanied by natural earthquakes. Turning to changes related with gas production, depletion-induced mechanisms are outlined in Sect. 3. We take over inversions of seismograms, but do not follow some assumptions of reservoir engineering.

Three subsequent sections of our paper deal with rock samples which exhibit scale-independent features of critical phenomena and their relics and serve therefore as *analogue models*. Multi-stage triaxial tests with sandstone samples yield patterns of shear bands with aligned cracks which similarly occur in the lithosphere (Sect. 4). Such patterns arise quasi-statically with dilatation up to a collapse with contraction, which corresponds to driven and spontaneous tectonics in the lithosphere. Changes of the rock fabric are also revealed by means of X-rays and micro-seismicity, respectively (Sect. 5), while elastic strains can be derived from the diffraction of neutron beams (Sect. 6).

The findings are of use not only for gas fields (Sect. 7). Our paper is disruptive and constructive, the arguments are

inductive and deductive. We try to overcome the present partially incompatible subdivision of Earth sciences by means of a unified approach. Conclusions follow in Sect. 8 together with an outlook, while mechanical and mathematical details are outlined in an appendix.

2 States and evolution before gas production

The region of interest was explored with hundreds of boreholes and thousands of seismic profiles [8]. A geological map (Fig. 1) exhibits tectonic structures which arose by normal and strike-slip faulting. Thus, depicted main faults have a distance from about 2 km to 10 km. Profiles obtained by means of P-wave travel times and borehole loggings (e.g., Fig. 2) indicate dislocations of layers along steep main faults. Minor faults and faults below about 3 km depth are thus not detected as P-waves intruded from above are blurred. Offsets in the upper Zechstein layer—consisting of mudstone and rock salt—produced grabens (ditches) and horsts (rifts) which were covered by tectonically less structured sediments. Layers of volcanic ash below indicate similar tectonic dislocations which traverse also a Carboniferous layer. The fractality is
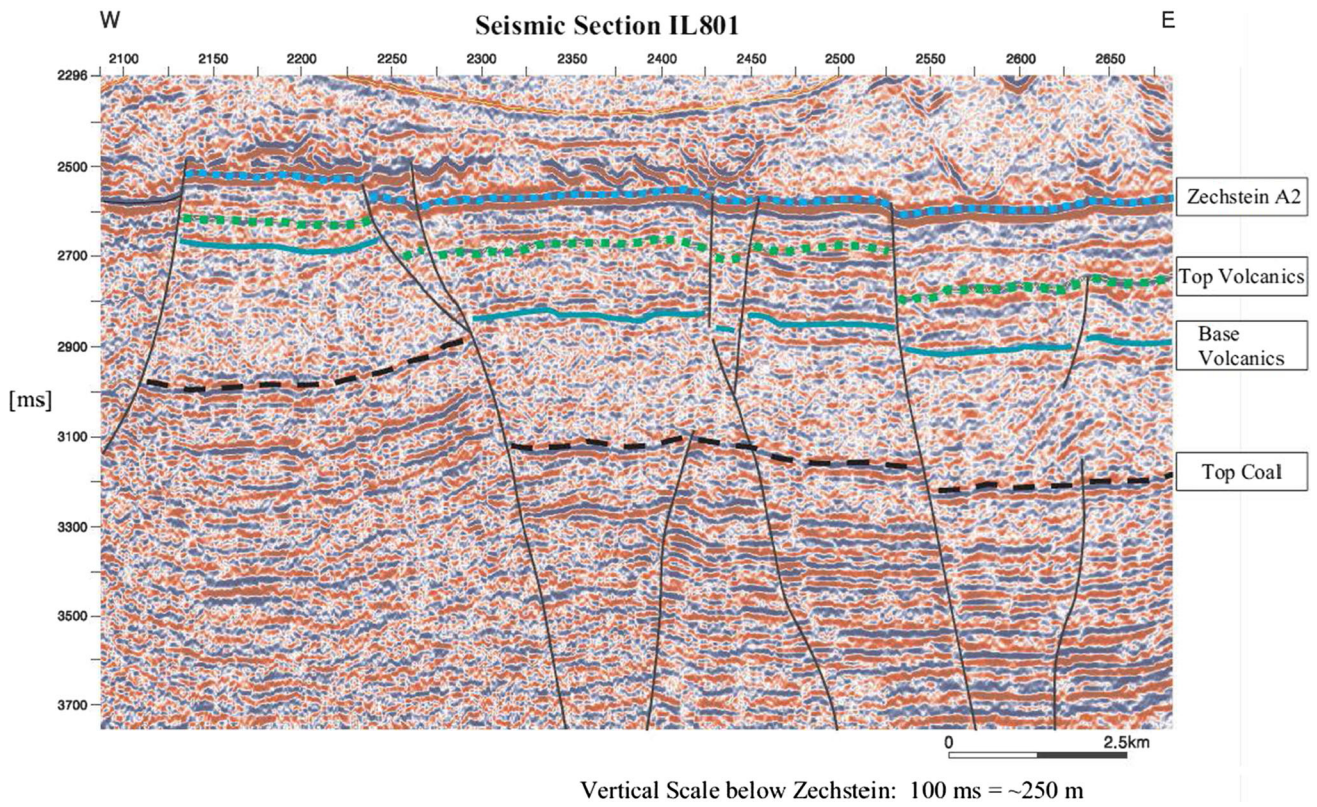
Fig. 2 A seismic profile of the site in Fig. 1 ([8],courtesy R Gast). Vertical travel times yield depths exaggerated by a factor of about 2 as they would imply $c_p \approx 11$ km/s
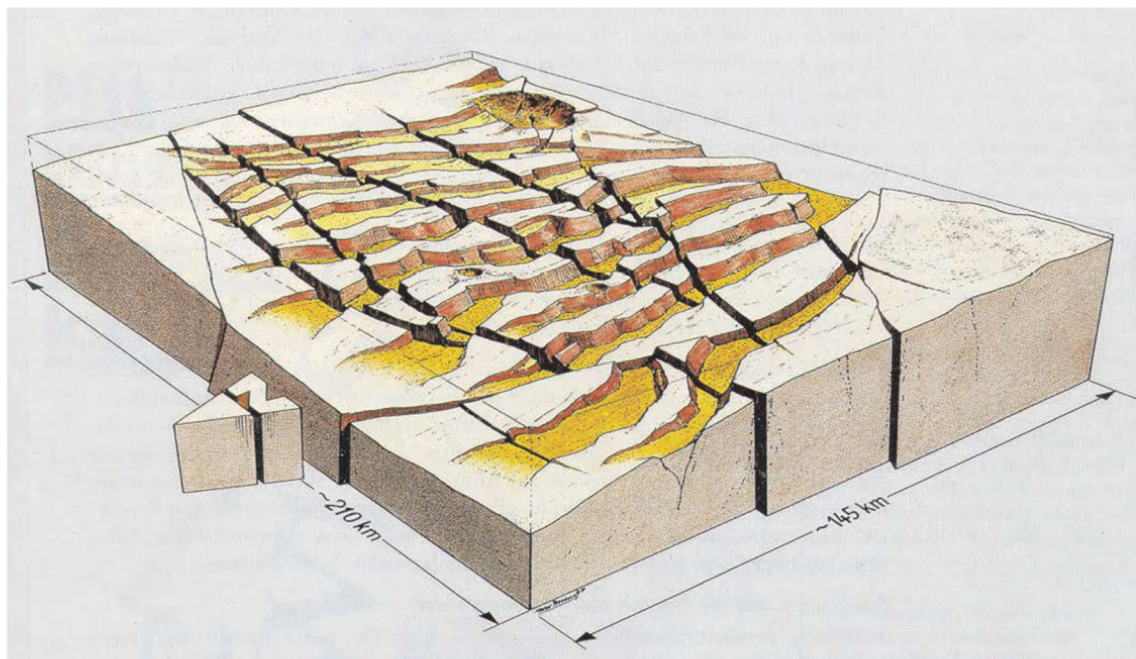
Fig. 3 Graben system almost 300 million years ago, reconstructed for the region shown in Fig. 1; vertical scale exaggerated ([8], courtesy R Gast)

indicated in a similar formation by fluctuations of density along almost horizontal boreholes under the North Sea with wavelengths from ca 10 m to 3 km [16].

A 3D reconstruction of a configuration almost 300 million years ago (Fig. 3) was worked out by Gast [7] for the same site. In addition to normal faulting with grabens and horsts, it exhibits an intra-plate strike-slip faulting (indicated by black lines with offsets), and a caldera from a volcanic eruption. It appears that the lithosphere was lifted by the magmatic basement so that the upper half of the Earth's crust was extended horizontally and sheared with occasional volcanic eruptions, except for the southward rim of the upheaval where it was shortened. Thereafter the basement presumably turned into a depression so that the upper half of the crust was shortened horizontally, while it was extended near the rim of the arising basin. The grabens were subsequently filled with sand, which was later converted into sandstone. Volcanite layers from Ireland to Poland speak for vast eruptions, salt and dust sedimented after the access of sea water and later converted into rock salt and mudstone, respectively.

More recently, the tectonic evolution was influenced by repeated glaciation and deglaciation [31]. Glaciation caused an increasing depression so that therein the upper half of the crust was compressed and its rim was extended, while deglaciation caused the reverse kinematics. The present wide-range heave indicates roughly the same rate of overall lithosphere reconfiguration as by the continual upper mantle motion so that both tectonic drives cannot be disentangled. In about 1/10 of the considered area, Zech-stein layers evolved into diapirs which caused faulting of overlying formations [21, 17]. Except these shallow structures, tectonic critical phenomena led to rather fractal

patterns with main faults of about 2 km to 10 km distance, which generated gas inclusions in the following way.

Mudstone layers were transformed along faults into *clay smears*. Such sealing bands with clay mineral attain a thickness of ca 1/10 of the source layer thickness and are disintegrated beyond a dislocation of almost 10 times the same thickness [34]. Despite their disintegration thinner clay smears, fed from minor mudstone layers, can overlap in main faults so that they also form seals. Intact mudstone layers and faults with overlapping clay smears can combine into *caprocks* if suitably oriented faults form a curtain all around. Profiles as, e.g., Fig. 2 (though not reaching deeper than about 3 km) confirm that caprocks could thus evolve. Clay smears in strike-slip faults—visible in Fig. 3 and less markedly by W-E-oriented parts of faults in Fig. 1 - could form northern and southern curtain parts of caprocks.

Gamma ray logs in a borehole for the Söhlingen gas field (middle of Fig. 1) indicate sandstone from ca 4.8 km to 5.4 km depth with thin interrupted mudstone inclusions, a major mudstone layer above and a volcanite zone with pervious faults below [8]. Natural gas, generated in the deeper Carboniferous, rose through the volcanite zone and was caught in sandstone by caprocks. Displaced water percolated through them, but no gas due to the high capillary entry pressure of mudstone. The gas fields in Fig. 1 have irregular shapes due to the multi-fractal fault pattern.

The *pore water pressure* p_w, measured at the bottom of boreholes, was up to almost 1/3 higher than the hydrostatic p_{w0} in the gas reservoirs before their depletion [24]. Off gas inclusions $p_{w0} \approx \gamma_w z$ hold with depth z and the groundwater table just under the surface, therein $\gamma_w \approx 11$ kN/m^3 is elevated by dissolved salt. p_w in a gas inclusion at rest is nearly depth-independent and equals the gas pressure p_g as the specific weight of gas is far below the one of water, and as the capillary entry pressure $p_c = p_g - p_w$ of sandstone is far below p_w. Above the caprock p_w is hydrostatic as long as there is no further seal, i.e., $p_w \approx p_{w0} = \gamma_w z$. The lateral curtain is simplified in Fig. 4, therein hydraulic equilibrium requires $p_w = p_{w0}$ at the lower bound of a gas inclusion as there is no seal. With $p_w \approx 1.3 p_{w0}$ this bound lies about 1.5 km deeper than the caprock at ca 4.8 km depth, so it lies in the permeable volcanite formation as the sandstone formation is ca 0.6 km thick. Different to the usual assumption in reservoir engineering [25] the distribution $p_w(z)$ is thus not linear for gas fields.

In a continuum image, the field of the *effective stress tensor* $\sigma'_{ij}(x_i)$ is related with p_w and the total stress tensor σ_{ij} by $\sigma'_{ij} = \sigma_{ij} - p_w \delta_{ij}$ (with unit tensor δ_{ij} and positive normal components for pressure). This relation was proposed for limit states of water-saturated soil by Terzaghi [30], and can be derived from the neutrality of the solid mineral with regard to changes of p_w also for rock [12].
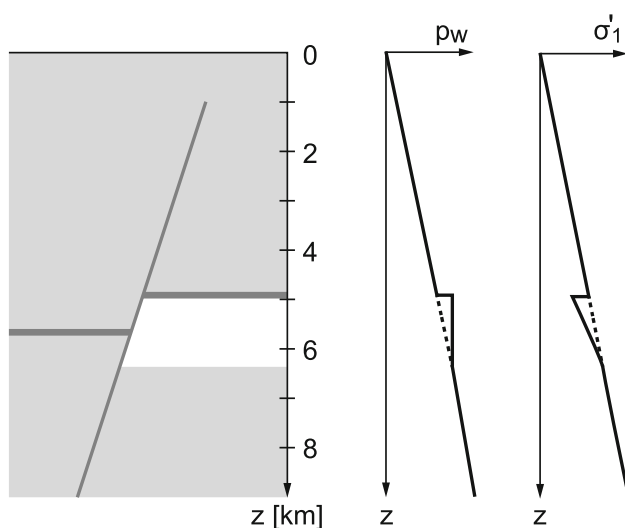
Fig. 4 Simplified cross section with a main fault and a gas inclusion (white), pore water and vertical fabric pressure versus depth
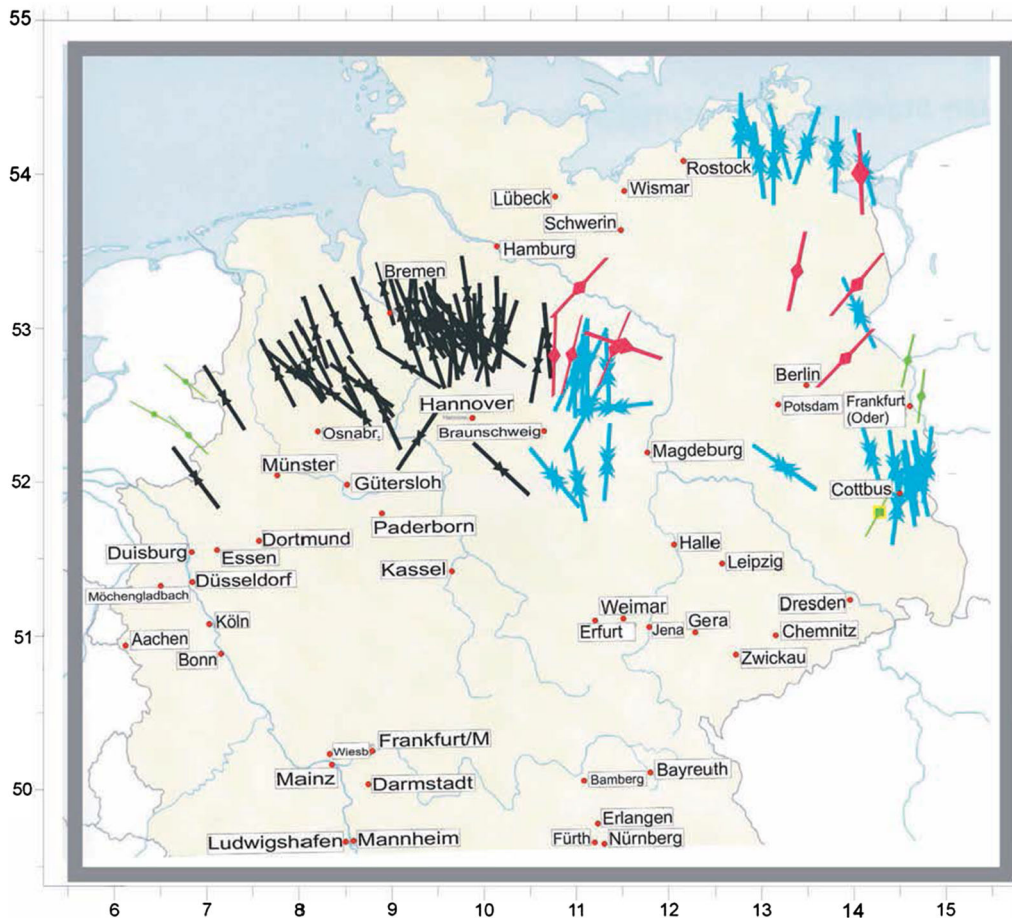
Fig. 5 Directions of major horizontal stress of the North German Basin for depths from 1 km to 7 km [27]. Different arrows denote different kinds of evaluation of borehole data by various authors

Taking the pressure of pore gas p_g instead of p_w, it is likewise legitimate with an inter-connected gas-filled pore system due to a capillary entry pressure $p_c \ll p_g$. For our region with a horizontal surface and normal plus strike-slip faulting the vertical stress is close to the major principal value of σ_{ij} from the overburden, i.e., $\sigma_1 \approx \sigma_{zz} \approx \bar{\gamma}z$ holds with average gross specific weight $\bar{\gamma}$ and depth z. The effective major principal stress is thus $\sigma_1' \approx \bar{\gamma}z - p_w$. Off gas inclusions this means $\sigma_1' \approx (\bar{\gamma} - \gamma_w)z$ by hydrostatic uplift, but a further reduction of σ_1' arises within and decreasingly below a gas inclusion (Fig. 4).

Strictly speaking, internal forces of rock cannot be captured by a Cauchy stress tensor σ_{ij}, but a *quasi-local* stress tensor $\hat{\sigma}_{ij}$ is legitimate (Note N1 in the Appendix). Reconfigurations with tectonic dislocations are no deformations as spatio-temporal distributions of displacements are not differentiable, and as there are no objective reference configurations. Quasi-local quantities are spatial averages of inspection cubes which are big enough for having fractal features, and small enough for being fractally uniform. Analogously, *quasi-momentary* quantities

are temporal averages of inspection intervals which are long enough for showing fractal features, and short enough for being fractally stationary. In this sense, elastic strain $\hat{\epsilon}_{ij}^e$ and pore volume fraction $\hat{n}$ are also quasi-local and -momentary. Non-fractal trends can be captured by means of fractional derivatives, which require an objective scaling so that units of length and time do not matter (N2).

The intermediate principal stress $\hat{\sigma}_2$ of tectonic extension and strike-slip zones is usually assumed to have the same direction as the maximal horizontal shortening, which can be estimated from caving-in boreholes by means of calipers. Directions of $\hat{\sigma}_2$ for depths from ca 1 km to 7 km in N-Germany, worked out by Röckel and Lempp [27], exhibit an overall NNW-SSE direction of σ_2 with spatial fluctuations for our region of interest (Fig. 5), which matches roughly the regional directions in the World Stress Map [15] and the ones of main faults in Fig. 1. Hydraulic fracturing, employed in the same study for getting the smallest principal stress $\hat{\sigma}_3$, is contestable as fractal features are not taken into account (Note N3), but there is no practicable alternative of the standard evaluation.
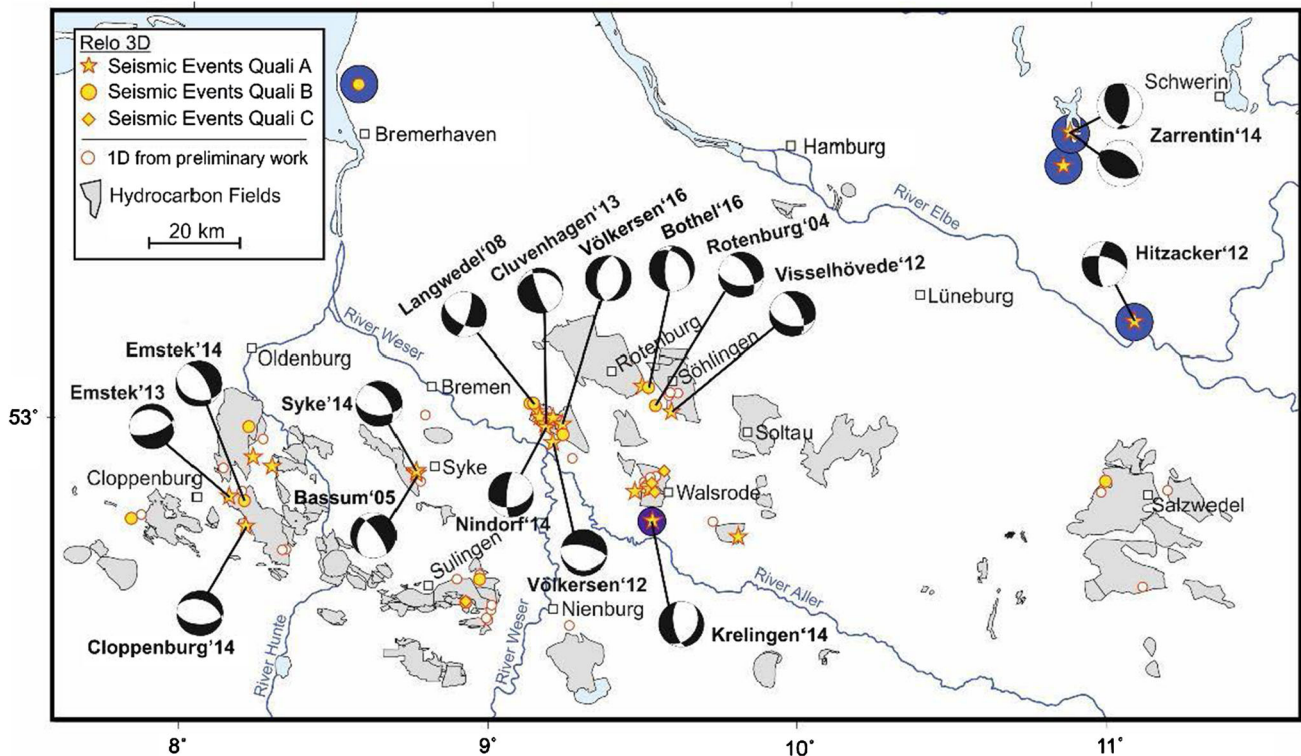
Fig. 6 Epicenters of seismic events with beach balls, denoted by names of nearby settlements and years of occurrence; quality symbols as in Fig. 1 ([31], courtesy P Uta)

The *natural seismicity* indicates that collapsible states of the solid fabric arise sporadically in our region of interest. Sources of recent natural earthquakes with magnitudes up to about 4 were localized by inverting seismograms ([31], blue circles in Fig. 1). Thus, determined depths range from about 5 km to 45 km with a lower precision than for the horizontal localization. Historical reports since the Middle Ages point to stronger earthquakes with longer recurrence times. The onset of a seismogenic loss of equilibrium indicates a collapsible state of the solid rock fabric, which is roughly captured by a Mohr–Coulomb condition with quasi-local quantities, whereas the usual assumption of a local sudden stress drop as seismic source is over-simpli-fied (N4).

3 Changes related with gas production

Earthquakes occurred more often in the considered region with the depletion of gas inclusions. Seismograms from stations installed for getting seismic profiles enabled a localization of depletion-induced seismic sources. This was achieved by Uta [31] with inversions of seismograms including spatial distributions of P-wave velocities. The resulting map shows epicenter sites, clustering near gas

fields, with so-called *beach balls* (Fig. 6). These are lower hemisphere stereographic projections of fault plane normals and directions of seismogenic dislocations at faults, derived with the classical theory of wave propagation and the assumption that waves are generated by a sudden
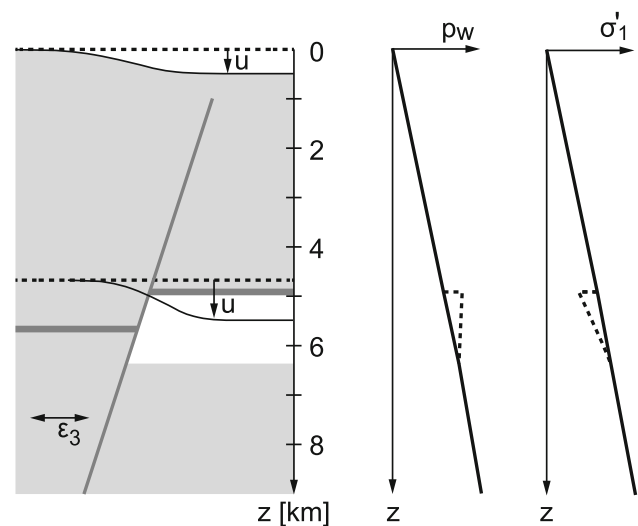
Fig. 7 Simplified cross section after depletion, with distributions of pore water and vertical fabric pressures versus depth and horizontal distribution of subsidence below the caprock and at the surface. Dashed lines from Fig. 2 indicate states before depletion

shearing with a stress drop (Note N4). Positions of beach balls are approximate epicenters derived from correlated P-waves arriving at different stations.

Normal faulting is represented by two opposite crescents, their secant having the direction of maximal horizontal shortening, and strike-slip faulting by two opposite black triangles, one diagonal having the azimuthal direction of the fault plane. For instance, the beach ball for Völkersen '16 in Fig. 6 indicates normal faulting with a NNE-SSW outcrop, Langwedel '08 points to strike-slip faulting with a NNW-SSE maximal shortening, while almost all the other depletion-related beach balls indicate combinations of both modes with different directions of main horizontal shortening. Despite spatial fluctuations, these directions come fairly close to the ones of main faults in Fig. 1 and of main horizontal shortening in Fig. 5.

Depletion-induced events (Fig. 6, blue circles for natural events as in Fig. 1) have source depths which range from about 4 km to 8 km [31]. The technically induced seismic activity is delayed against the depletion by almost 20 years [24]. Similar delay times were observed in other gas fields by Grasso and Wittlinger [9] and van Eck et al. [33]. Combinations of the lowest principal stress $\hat{\sigma}_3$—obtained by hydraulic fracturing at the bottom of production wells— with $\hat{\sigma}_1 = \bar{\gamma}z$, and subtracting the pore water pressure p_w, indicate a proximity to collapsible states [24].

For comparison, let us consider the seismicity induced by *injection*. In the well-known case of the Rangely oil field in Colorado water was injected for enhancing the oil production, this led to seismic events with magnitudes up to about 4. Haimson [14] proposed an explanation by means of hydraulic fracturing, arguing that the effective Mohr stress circle for the employed borehole near a main strike-slip fault was shifted towards the τ-axis so that a Coulomb tangent with $c' = 0$ was reached. Cracks observed in the borehole indicate a direction of the lowest principal stress σ_3 as by fault plane solutions. However, a cluster of epicenters arose only SW of the borehole near the opposite rim of the oil field, which indicates sources off the main fault with a fractal spatial distribution.

With a *depletion* Mohr circles should analogously be shifted further off the τ-axis, so how and where could earthquakes be induced? Values of σ_3 in ca 4.8 km depth, obtained with hydraulic fracturing at the bottom of production wells for different times in one gas field, exhibit fluctuations and a reduction near the rim [24]. It is often supposed [25] that the rock fabric can get critical by depletion in the middle of gas fields, and that the ratio of increments of pore water pressure Δp_w and of smallest horizontal pressure $\Delta \sigma_3$ by depletion is nearly constant. Both assumptions are questionable (Note N5 in the Appendix), whereas a seismogenic mechanism can be derived by comparing a simplified cross section after the depletion (Fig. 7) with the one before (Fig. 4). While $p_w \approx p_g$ is higher than hydrostatic in a gas inclusion, and therein almost depth-independent, it is hydrostatic elsewhere and gets so where gas is replaced by water with the depletion. Thus, the vertical effective stress σ_1' grows were gas is extracted, and less with the spread distribution of additional stress also below up to a depth of about 1/3 of the distance of cap-confining faults.

This change of state is accompanied by—but not uniquely related with—a vertical shortening of the solid fabric in and below the interior of the caprock as there the effective principal stress components increase. The resulting vertical displacement forms a trough which is wider spread at the free surface than just under the caprock. Thus, the rock mass near the rim of the subsidence trough is *stretched horizontally* mainly in a depth near the one of the depleted gas inclusion, so that there—as far as a naturally driven tectonic horizontal stretching is enhanced in the same direction—collapsible states can be reached (like at the rim of a depression from the magmatic basement or by glaciation, Sect. 2). Not in main faults with overlapping clay smears, however, as with their low activation energies stress deviators are more rapidly relaxed than generated by the slow tectonic reconfiguration, but in minor nearly parallel faults with a harder mineral.

The argument with Figs. 4 and 7 leaves aside spatial fluctuations. Moreover, cross sections with caprocks are not symmetric, and different sediments lead to more or less sealing clay smears. Configurations with layers and faults, and distributions of quasi-local stress and pore water pressure, cannot be precisely determined with seismic profiles and borehole logging. Gas inclusions arose in a tectonic-sedimentary setup which led to caprocks and gas inclusions with about 2 km to 10 km width like the distances of main faults (Sect. 2). The latter match *corner frequencies* of seismic spectra (e.g., Fig. 8). Therein amplitude denotes the square u_a^2 of displacement amplitude u_a, obtained by integration of the registered velocity v. Both are related by $v = 2\pi f u_a \cos(2\pi f t)$ for each frequency f so that u_a^2 is proportional to v_a^2 and to f^{-2}.

It can be shown with the fractional calculus (N2) that spectra of waves propagating in a fractal solid tend to $v_a^2 \propto f^{-2\alpha}$ with an exponent 2α just below 2. Only for this narrow α-range wave crests with their polarization propagate almost independently of fractality, though with a dispersion in the elastic range, therefore the inversion of seismograms with the classical wave theory works approximately. The negative slope of $\log u_a^2$ versus $\log f$ should be just below 4, but it is bigger in Fig. 8 and in further spectra presented by Uta [31]. This deviation is presumably due to a filtering which reduced amplitudes more for high than for low frequencies, but does not distort corner frequencies f_c.
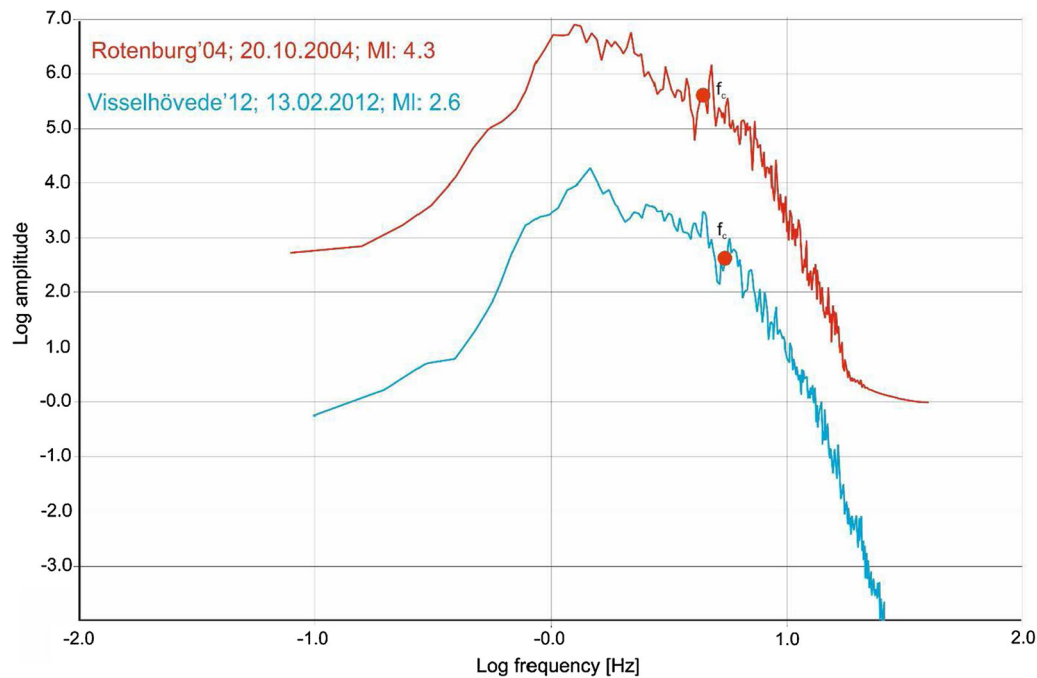
Fig. 8 Spectra of a natural and a depletion-induced earthquake in the middle of the region of Fig. 6 ([31], courtesy P Uta). Amplitude means square of displacement, corner frequencies are derived from linear approximations of log-log plot sections

Uta [31] obtained f_c from about 3 to 6 s^{-1} for depletion-induced events with source depths of about 5 km, and from about 5 to 10 s^{-1} for natural events from about 20 to 30 km depth (visible, e.g., in Fig. 8). Assuming shear wave speeds $c_s \approx 3$ km/s for 5 km and ca 5 km/s for 25 km depth, the corner wavelength $l_c = c_s/f_c$ is thus about 1 km both for shallow and deep sources. These are no lower bounds, the left ends of the plateaus in Fig. 8 from about $f_c/10$ to $f_c/5$ indicate wavelengths from about 2 to 10 km. The latter range matches depth-independent major fault distances from about 5 to 20 km. They delimit the size of depletion-induced seismic source regions, which is confined by the length of inclusion rims with an orientation close to the one of main faults.

Corner frequencies indicate the magnitude of seismic events although plateau amplitudes and widths are not strictly correlated with magnitudes. The delay of induced seismicity versus depletion by almost 20 years arose as only with a sufficient stretching by bending rock near the rim of gas fields could reach collapsible states. The conclusion of Müller et al [24], viz. that depletion-induced earthquakes cannot exceed magnitudes up to ca 3, is thus confirmed. Following Uta et al [32], the earthquake Rotenburg 2004 (Fig. 6, middle) with a magnitude of 4.3 was not depletion-induced as a neighbored one occurred later with a shallower source. However, triggering major natural earthquakes by depletion is not excluded generally.

These findings confirm that seismicity arises in *chain reactions* [11]. The first attained collapsible zone loses equilibrium with a contraction of the pore system, thus the pore water pressure p_w rises suddenly so that a P-wave arises with an initial pressure increase. The rapid rise of p_w makes the surroundings collapsible as far as it was already nearly so, and alongside with triggering seismic waves a chain reaction evolves up to its blockade by a more stable surroundings. Thus, generated P- and S-waves get longer and higher as far as the state before is almost collapsible and the stress alignment is rather uniform (like with dominoes on a table). Arrival times of P-waves enable a localization of initial sources (N4), while slower S-waves radiate more energy than P-waves so that they dominate power spectra.

Müller et al [23] employ analytical methods with *poroelasticity* for showing how stress states of the solid rock fabric can get critical. Therein the fabric is considered as an elastic continuum, and the fluid in the pore system is also assumed to be elastic. The interaction of solid and fluid is captured by Biot's relation (which is contestable, Note N6). Like with the natural tectonic bending of lithosphere sections [31], delayed approaches to collapsible states can thus be qualitatively explained, especially near injection boreholes or at the rim of subsidence troughs. However, tectonic evolutions with driven and spontaneous critical phenomena elude as yet largely such a mathematical treatment as both are mainly inelastic [11].
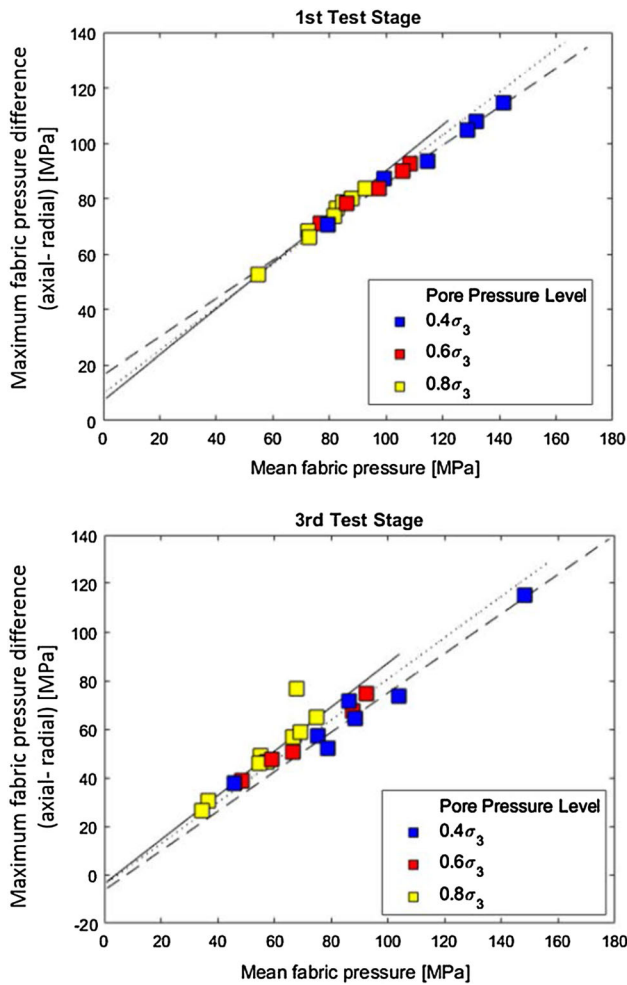
Fig. 9 Limit stress states of water-saturated sandstone samples, attained in multi-stage triaxial tests (modified after [18]). Deviators versus spatial mean values of overall stress minus pore pressure at one endplate

4 Multi-stage triaxial tests

Multi-stage triaxial tests with water-saturated sandstone samples were carried out by Lempp et al [18]. In one series, with samples of 7 cm diameter and 14 cm height, limit states were repeatedly attained with gradually increased confining pressure $\hat{\sigma}_3$ by axial shortening up to a sudden drop of the mean axial average stress $\hat{\sigma}_1$. A disintegration of the sample was prevented by means of a servo-hydraulic device, thus limit states were repeatedly attained with gradually higher $\hat{\sigma}'_3$. Equalizing the pore water pressure p_w at the top plate with its spatial average $\hat{p}_w$, effective stress components $\hat{\sigma}'_1 = \hat{\sigma}_1 - \hat{p}_w$ and $\hat{\sigma}'_3 = \hat{\sigma}_3 - \hat{p}_w$ were calculated for limit states. Plots of such collapsible states, obtained with samples cut from a block, scatter around straight lines for each stage (Fig. 9). They can be approximated by the Mohr–Coulomb condition

$$\hat{\sigma}'_1 - \hat{\sigma}'_3 = (\hat{\sigma}'_1 + \hat{\sigma}'_3)\sin\phi' + 2\hat{c}' \tag{1}$$

with an effective friction angle ϕ' and an effective overall cohesion $\hat{c}'$. Despite scattering Fig. 9 confirms the principle of effective stress as losses of equilibrium—depending on $\hat{\sigma}'_1$ and $\hat{\sigma}'_3$—were likewise attained with different levels of $p_w/\hat{\sigma}_3$. $\hat{c}'$, estimated by extrapolation to $\hat{\sigma}'_3 = 0$, dwindles from ca 10 MPa for the first stage (Fig. 9) to nearly 0 in the third one (below), while ϕ' (represented by the slope) dwindles but slightly. In a few tests—not depicted in Fig. 9—intact samples were stressed with $\hat{\sigma}_3 = 0$ or $\hat{\sigma}_1 = 0$ up to axial splitting or discing, respectively. Such fractures cannot be captured with (1) as this equation is confined to shear ruptures.

More sophisticated tests were carried out with samples of 10 cm diameter and 20 cm height. Collapsible states were again repeatedly attained with axial shortening, sometimes by increasing p_w at the top plate with constant axial force and confining pressure (e.g., Fig. 10). Overall deformations were measured by gauges at the sample, axial ones were used for the servo-control. Overall volume changes, measured via taken up or squeezed out pore water, exhibit a *driven dilatation* alongside with an imposed increase of $\hat{\sigma}'_1$, up to a collapse with a *spontaneous contraction*. Each collapse is announced by a crackling noise and a temporary rise of p_w at the top plate.

After the test, the sample was unloaded and its cylindrical surface was unwrapped, then photographs were taken and combined into strips (e.g., Fig. 11). Visible shear bands are brighter from crushing of grains by mutual rotations, and hatched smaller shear bands indicate spatial fractality. Such patterns could not arise near the endplates as these prevent offsets, and likewise near the sample axis. Like with sand [2], the shear bands have an inclination $\theta \approx \pm(45^0 - \phi'/2)$ versus the axis. Invisible minor cracks opened near the endplates with driven axial shortening, closed with a reduction of $\hat{\sigma}_1 - \hat{\sigma}_3$, and so on in stages, while cracks aligned with shear bands opened visibly only by total unloading. All that happened in tests with $\hat{\sigma}'_3 > \hat{c}'$, otherwise cracks dominated.

Dilatant tests stages with $\hat{\sigma}'_3 > \hat{c}'$ can be captured by the *stress-dilatancy relation*

$$\frac{\hat{\sigma}^f_1}{\hat{\sigma}^f_3} \equiv \frac{\hat{\sigma}'_1 + \hat{p}_c}{\hat{\sigma}'_3 + \hat{p}_c} = -2\tan^2(\pi/4 + \phi'_0/2)\frac{d\hat{\epsilon}^i_3}{d\hat{\epsilon}^i_1}. \tag{2}$$

Extending the relation for sand [28], an additional pressure $\hat{p}_c$ of the fabric from the traction of cohesive bridges is employed which is equivalent to $\hat{c}' = \hat{p}_c\tan\phi'$ [11]. The observed increase of $\hat{\sigma}'_3/\hat{\sigma}'_1$ with an increase of $-d\hat{\epsilon}_3/d\hat{\epsilon}_1$, obtained by combining smoothed-out plots of $\hat{\sigma}'_1$ and $\hat{\epsilon}_3$ versus $\hat{\epsilon}_1$ [22], is matched by (2) with growing ϕ' and $\hat{p}_c$ for each stage, while the collapse amounts of both dwindle
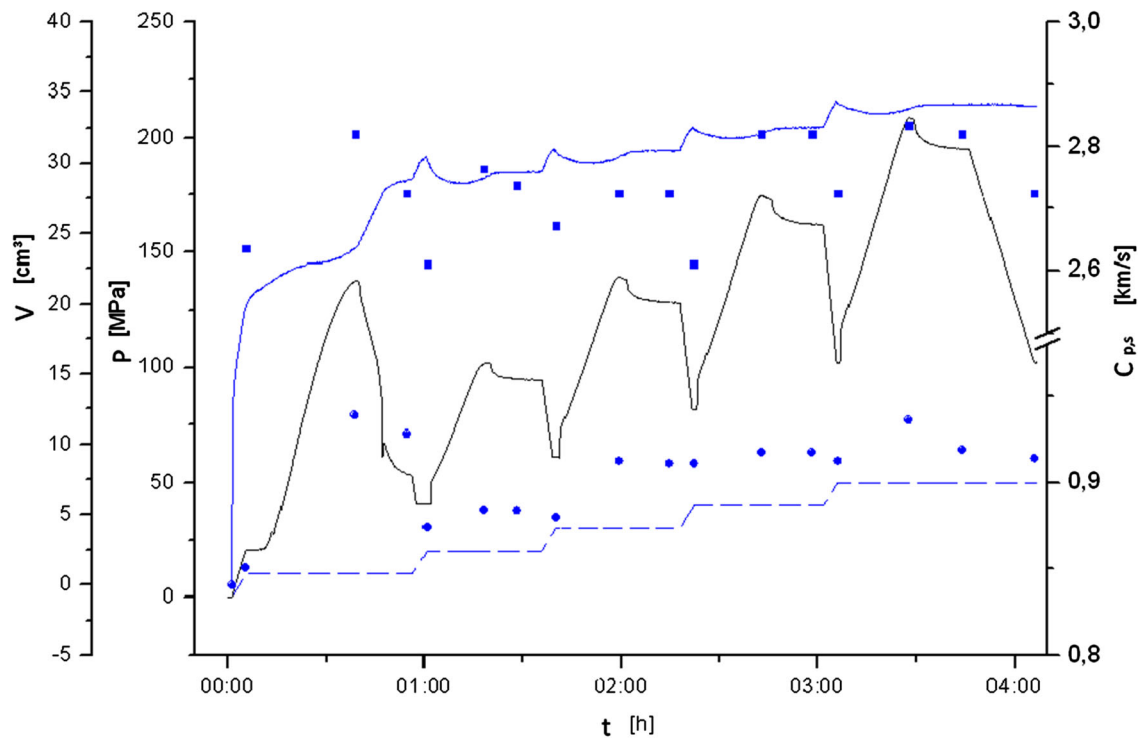
Fig. 10 Axial (middle line) and confining (dashed line) effective pressures, pore volume (upper line), and speeds of P- and S-waves (squares and dots, respectively), versus time in a multi-stage triaxial test with water-saturated sandstone (Lempp, internal report)

Fig. 11 Unrolled combined photographs of a sandstone sample after a multi-stage triaxial test with $\hat{\sigma}_3' > \hat{c}'$ [18]

slightly and strongly, respectively, in successive stages (visible in Fig. 9). In one test, e.g., a collapse occurred repeatedly after a dilation up to the pore volume fraction

$\hat{n} \approx 0.11$. The driven succession of critical points can be represented by saddle points up to an $\hat{n}$-dependent threshold of the specific energy with regard to elastic strain
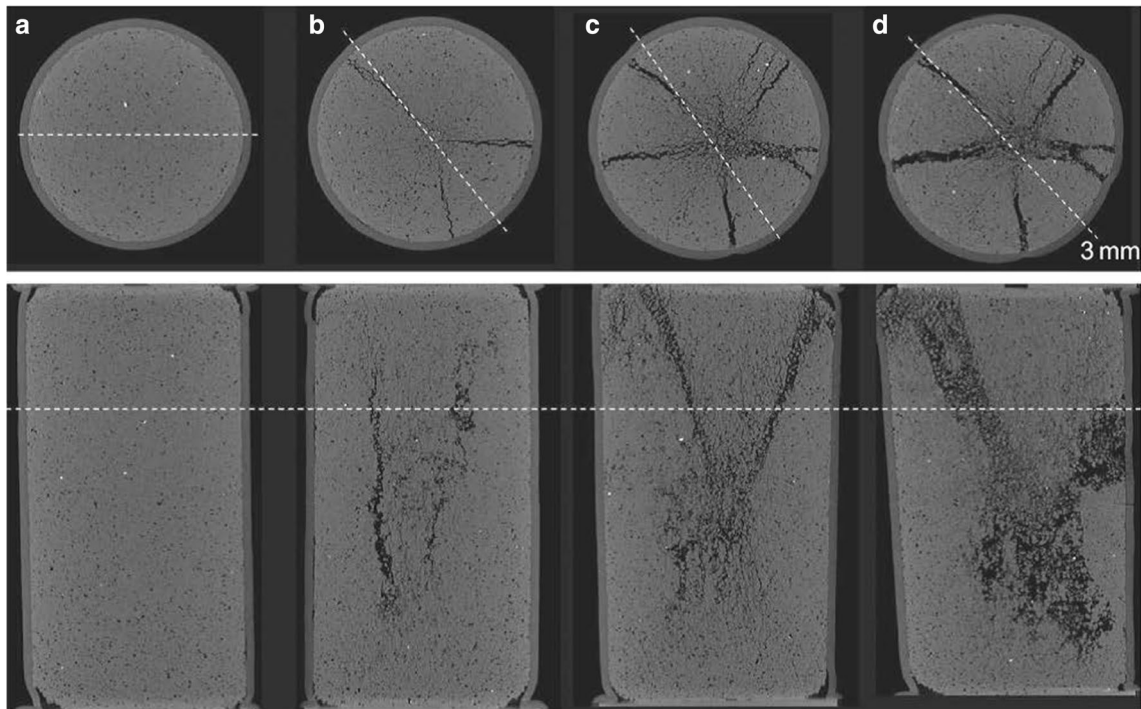
Fig. 12 X-ray tomographies of a dry Fontainebleau sandstone sample in a triaxial test ([3], courtesy C Viggiani). Stages from left (a) to right (d) are outlined in the text

invariants [11]. The same constitutive model captures dilatancy, contractancy and non-critical states in between also without axial symmetry.

5 Triaxial tests with X-ray tomography or seismometry

The *attenuation of X-rays* can reveal cracks and shear bands in a rock sample. Fonseca et al [3] present tomographies with voxel sizes of 8.5 μm from dry sandstone samples with 11 mm diameter and 22 mm height in triaxial tests. In one of them (Fig. 12), with $\hat{\sigma}_3 = 2$ MPa, an initially intact (a) axially shortened sample reveals first some radial cracks near the mid-plane (above) and nearly axial cracks in a vertical cut (below) prior to a peak with $\hat{\sigma}_1 \approx 60$ MPa (b). After a sharp drop to $\hat{\sigma}_1 \approx 20$ MPa further radial cracks appear while arising shear bands delimit a cone under the top plate (c), thereafter further shortening leads to $\hat{\sigma}_1$ near 10 MPa and to widening shear bands, while cracks are partly closed and erased (d).

The peak state can be captured by (1) with $\phi' \approx 45^0$ and $c' \approx 14$ MPa, so this sandstone resembles the intact one represented by Fig. 9 (above). With these estimates, plus $\hat{\sigma}'_1$ and $\hat{\sigma}'_3$ as given above, $\hat{\sigma}'_3 < \hat{c}'$ holds up to the peak and cracks dominate, whereas after the peak the state turns to

$\hat{\sigma}'_3 > \hat{c}'$ and shear bands dominate. The X-ray tomographies by Fonseca et al [3] confirm thus the discrimination outlined in Sect. 4, though but crudely with a single test stage. $\hat{\sigma}'_3 > \hat{c}'$ characterizes likewise tectonic evolutions with dominating faults, also with technical enhancement, while $\hat{\sigma}'_3 < \hat{c}'$ characterizes rockbursts near pressure-free surfaces or by injection (Sect. 7).

Turning to triaxial tests with *seismometry*, we consider first the axial propagation of imposed waves for different states of a sample. For instance, Fig. 10 shows velocities c_p and c_s of P- and S-waves from the upper to the lower endplate in a multi-stage test. Apart from fluctuations c_p and c_s grow with an increase of $\hat{p}' = (\hat{\sigma}_1 + 2\hat{\sigma}_3)/3$, and drop again when $\hat{p}'$ drops after a confined collapse, whereas their reduction by dilatation is compensated by the growth of $\hat{p}'$. These changes match the constitutive model proposed by Gudehus and Lempp [11], and with it spatial distributions of c_p in our gas fields match also the ones assumed by Uta [31] for localizing seismic sources (Sect. 2 and 3). However, the amounts of c_p in Fig. 10 are about half the ones assumed by Uta [31], and those for evaluating Fig. 8, for the same range of $\hat{p}'$. This reduction can be attributed to an imperfect coupling at the endplates, so a better evaluation requires sensors along the confining membrane.

Wavelengths related with Fig. 10 equal roughly the sample diameter, so c_p and c_s are overall quantities. A more

detailed insight, also with seismicity arising in the sample, requires smaller wavelengths. For instance, Griffiths et al [10] employed them with dry sandstone samples by means of 14 piezo-electric transducers at the confining membrane of a triaxial setup. Thus, they tracked down micro-seismic sources along a major shear band, including its alignment. Adding pore water and measuring its pressure p_w and its in- or outflow, one could thus localize micro-seismic chain reactions which are enhanced by collapse-induced increases of p_w. Power spectra could indicate sizes of micro-seismic sources, and magnitude-related numbers of successive seismogenic chain reactions in multi-stage tests could help understand their probabilities [11].

Multi-stage triaxial tests with piezo-elements could also help understand the *shear wave splitting* (SWS). An S-wave, entering a solid with orthogonal anisotropy along its major axis and polarized along the principal plane with lowest shear stiffness, is split into an S-wave with the same polarization and a faster one with an orthogonal polarization for which the shear stiffness is bigger. Crampin and Peacock [1] explain SWS by means of penny-shaped micro-cracks aligned along the average major principal stress, and attribute its observed switch to a percolation of cracks at a critical point. However, triaxial tests–as, e.g., those represented by Fig. 11 or 12—show that cracks dominate only for $\hat{\sigma}'_3 < \hat{c}'$ (with quasi-local quantities), whereas shear bands dominate for $\hat{\sigma}'_3 > \hat{c}'$, and that fractal patterns arise up to a collapse in both cases [11].

The anisotropic elasticity needed for SWS can be achieved with $\hat{\sigma}'_3 > \hat{c}'$ in a central belt near the membrane of about 1/3 of the sample height (visible, e.g., in Fig. 11), and a thickness of about 1/4 of the sample radius like with sand [2]. Therein the radial stretching is about twice the circumferential one as the latter is independent of the radial angle ϑ in a horizontal plane, while the former dwindles towards the axis. Thus $\hat{\sigma}'_\vartheta < \hat{\sigma}'_r < \hat{\sigma}'_1$ is achieved within the belt, which ensues an orthogonal elastic anisotropy by the constitutive model of Gudehus and Lempp [11]. If an imposed S-wave is polarized in a plane $\vartheta = 0$ a faster S-wave arises in the belt with orthogonal alignment, while a slower S-wave propagates in the plane $\vartheta = 0$. A confined collapse leads to $\hat{\sigma}'_r < \hat{\sigma}'_\vartheta < \hat{\sigma}'_1$ within the belt, this causes a switch of SWS. Both kinds of SWS are obtained with fractality by means of a fractional eigenvalue problem, therein the stress-alignment results from successive driven critical points and relaxation by a confined collapse (Note N7). The potential of SWS in the lithosphere (outlined in Sect. 7) could thus be improved by means of lab experiments.
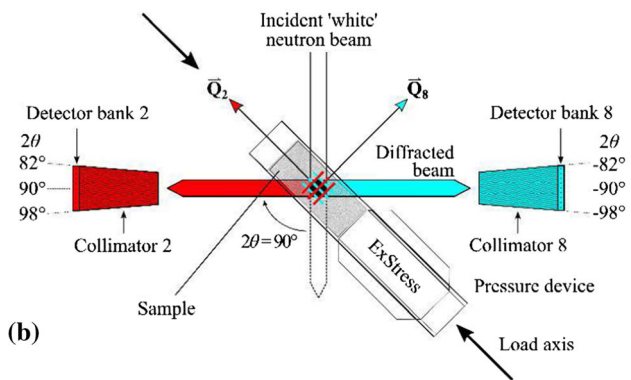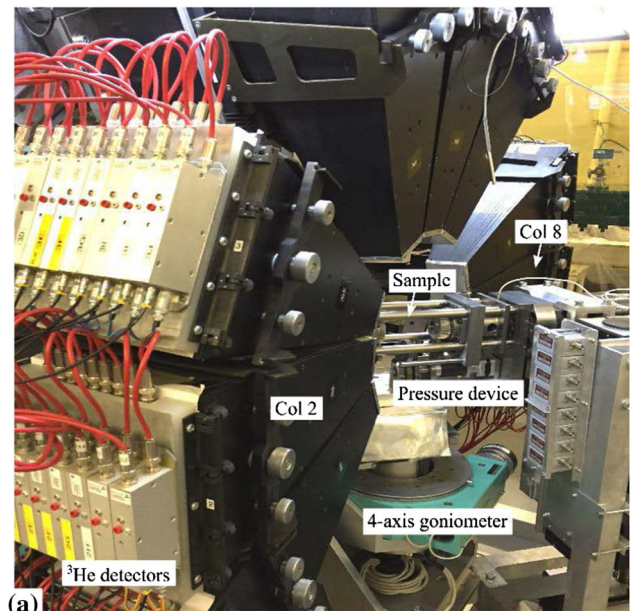
(a)

(b)

Fig. 13 Setup for experiments in Dubna/Moscow (Scheffzük, internal report). A neutron beam from a 107 m distant spallation source hits a gauge volume in the sample, this is kept in a loading device and positioned and aligned by a goniometer. Diffracted beams in nine directions are registered via collimators by 81 detectors, mounted in 9 banks with a horseshoe array. Bank 2 yields an average crystal lattice distance in the axial direction $\bar{Q}_2$ of the sample, bank 8 works for a transversal direction $\bar{Q}_8$

6 Diffraction of neutron beams

Stress distributions of rock samples cannot directly be observed, but the *diffraction of neutron beams* enables an observation of elastic deformations of crystallites through Bragg reflections (like 3D strain-meters based on fiber Bragg gratings), which in turn are related with stresses. If a single crystal has six differently oriented lattice planes with different distances, a neutron beam (which is mainly scattered by protons while X-rays mainly interact with electrons) is diffracted in six different directions with six lattice plane distances. The scattering angle between

arriving and diffracted beams of a crystal depends on wavelength and lattice plane distance by Bragg's relation. Changes of lattice plane distances cause diffraction line shifts for at least six directions, which can be transformed into six components of the elastic strain tensor.

Stress-free powder diffracts neutron beams in various directions like the crystal axes so that both scatter spatially, thus diffracted beams lie on a Debye–Scherrer cone for each crystal axis and lattice plane distance. Each diffracted beam can be recognized by a peak of its intensity versus time of flight of the neutrons (their wavelength is given by de Broglie's relation, while a high energy resolution is achieved by a pulsating neutron source). Six lattice plane distances of randomly aligned crystallites lead to at least six peaks of beam intensity. These peaks serve as reference for deformed crystallites in a solid, although this has dislocations and related elastic deformations which fluctuate with wavelengths near the sizes of crystallites. Despite the dispersion due to such spatially confined fluctuations changes of lattice plane distances, visible by peak shifts of the intensity of diffracted neutron beams versus time of flight, can yield an average elastic strain tensor $\bar{\epsilon}_{ij}^e$ for a gauge volume (Note N8).

We refer to observations at the Joint Institute for Nuclear Research in Dubna near Moscow (Fig. 13). A polychromatic pulsed neutron beam is delimited by slits and diffracted beams are focussed by collimators, thus a gauge volume is delimited in the sample, the position and orientation of which can be adjusted. Wavelengths of up to 0.7 nm enable to detect lattice plane distances up to 0.5 nm (sufficient for quartz). A gauge volume of 2 cm^3 was chosen for getting enough neutrons per unit of time with crystallite sizes up to 0.5 mm. Counts of neutrons detected in a diffracted beam (setting the diffraction angle to 90^0)

exhibit peaks versus times of flight, which are proportional to wavelengths and molecular energies. These peaks are shifted against the ones of annealed powder and indicate average elastic strains $\bar{\epsilon}_k^e$ for 9 directions $\bar{Q}_k$ or spatial unit vectors e_i^k. Each one of the 9 unit vectors e_i^k refers to a coordinate system given by the axis $\bar{Q}_2$ of the sample and a normal $\bar{Q}_8$. A set of at least six strains $\bar{\epsilon}_k^e$ for six directions $\bar{Q}_k$ can be transformed for the gauge volume into an average strain tensor $\bar{\epsilon}_{ij}^e$ as far as this is legitimate (Note N9).

Findings in Dubna with uniaxially loaded rock samples elude usual assumptions of materials science. Frischbutter et al [4] report that—differently from pore-free metal—crystal lattice strains of initially intact sandstone samples are smaller than elastic strains of the solid fabric as the pore system reduces the elastic stiffness of the fabric. Moreover, strains from different gauge volumes along sample radii exhibit wild fluctuations so that usual strain tensors serve at best as a first approximation. Frischbutter et al [5] observed similar fluctuations by means of successive gauge volumes along the axis of granite samples from a fault zone. Elastic strains got less uniform with an arising nearly axial crack, which was localized by means of seismometers at the cylindrical surface, and velocities of ultrasonic waves fluctuated likewise wildly. Scheffzük et al. (2015) [29] observed similar fluctuations with gneiss samples from a folding zone, and an acoustic emission which dropped by unloading.

For better understanding the depletion-induced seismicity, a novel triaxial cell was built and placed in the Dubna diffractometer setup. For avoiding the attenuation of neutron beams by hydrogen nuclei (protons), the confining membrane consists of a *TiZr* alloy and the pore fluid is heavy water (D_2O) instead of water (H_2O). In a precursor
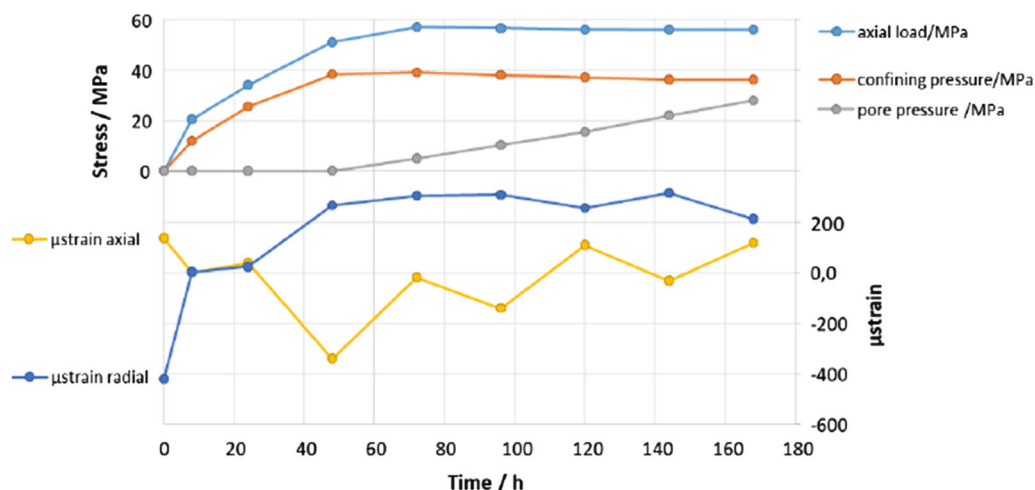
Fig. 14 Axial, confining and pore fluid pressures, imposed to a saturated sandstone sample in a novel triaxial cell (above); axial and radial changes of lattice plane distances in a central gauge volume detected by refraction of neutron beams (below) (F Schilling, internal report)

(Polsky et al. 2013) [26], water was pumped into a cylindrical rock sample with constant confining pressure (which cannot be controlled independently of the pore pressure) up to hydraulic fracture, and elastic strains were observed with two detector banks. In the novel device, which enables an independent control of axial force, confining pressure and pore water pressure, an initially intact sandstone sample with 3 cm diameter and 6 cm length was loaded in steps with a nearly constant ratio $\hat{\sigma}_1/\hat{\sigma}_3$; first without excess pore pressure p_w (relative to the atmospheric pressure), thereafter p_w was increased in steps while $\hat{\sigma}_1$ and $\hat{\sigma}_3$ were kept constant (Fig. 14). A minor relaxation of $\hat{\sigma}_3$ may be attributed to the triaxial device without servo-control.

Neutron beams, diffracted from a central gauge volume of 2 cm^3, were registered every few hours in rest intervals, and peaks of counts were evaluated for changes of lattice plane distances. In Fig. 14 (below) μstrain denotes average relative extensions of lattice plane distances, multiplied by 10^6, in the axial and one radial direction. They are registered by detector banks 2 and 8, respectively (Fig. 13), and named $\bar{\epsilon}_2^e$ and $\bar{\epsilon}_8^e$ in the sequel. Both differ from 0 at the onset, which indicates an eigenstress field of the sample as against stress-free powder, and vanish in the first interval, which can be attributed to a non-uniform stressing by the adaption of the sample to the endplates. The near-zero of $\bar{\epsilon}_2^e$ and $\bar{\epsilon}_8^e$ in the second interval is accidental.

In the next interval with a further increase of $\hat{\sigma}_1$ and $\hat{\sigma}_3$, but still $p_w = 0$, the radial $\bar{\epsilon}_8^e$ increases and the axial $\bar{\epsilon}_2^e$ decreases. This change appears qualitatively evident, but cannot be captured by a classical constitutive relation with uniformity and isotropy. In the continuation with increasing p_w, while $\hat{\sigma}_1$ and $\hat{\sigma}_3$ are kept constant, $\bar{\epsilon}_8^e$ and $\bar{\epsilon}_2^e$ evolve with growing fluctuations. Their amplitude is bigger for $\bar{\epsilon}_2^e$ than for $\bar{\epsilon}_8^e$, while both exhibit about the same period. Shorter intervals would reveal shorter periods, therefore the linear interpolation in Fig. 14 is simplified. A classically presumed reduction of $\bar{\epsilon}_2^e + 2\bar{\epsilon}_8^e$, and thus of $\hat{\sigma}_1' + 2\hat{\sigma}_3'$, is not attained [24].

The 9 detector banks of Fig. 13 enable principally the determination of six components $\bar{\epsilon}_{ij}^e$ of the spatially averaged elastic deformation of the crystallites in a gauge volume (Note N8 in the Appendix), though with a bias due to the orientation of the sample with regard to the horseshoe array of the detectors, and restricted as lattice plane distances are not changed by pure shearing. These shortcomings could be compensated by rotating the triaxial device also around its axis with a six-component support, counting neutrons for successive rotation increments. The intact sandstone for Fig. 14 was the one of Sect. 4, so micro-tectonic dislocations occurred more often with cracks than with shear bands due to $\hat{c}' > \hat{\sigma}_3'$. The growing non-uniformity and the high initial cohesion require multi-

stage tests, a scanning with smaller gauge volumes and a stronger neutron beam. After a reduction of $\hat{c}'$ below $\hat{\sigma}_3'$ shear bands would dominate. The symmetry $\hat{\epsilon}_{ij}^e = \hat{\epsilon}_{ji}^e$ is justified as otherwise estimates of principal directions of horizontal stress and shear wave splitting (SWS) would not work [11].

Thus multi-stage triaxial tests with diffraction of neutron beams could help clarify some fundamental questions. The transition from an average elastic strain tensor of crystallites ($\bar{\epsilon}_{ij}^e$) to the quasi-local one of the porous solid fabric ($\hat{\epsilon}_{ij}^e$) could be quantified with un- and reloading in the elastic range (N9), therein $\hat{\sigma}_{ij}'$ is related with $\hat{\epsilon}_{ij}^e$ via the specific elastic energy $\hat{w}_e$ with a reduction factor for the spatial fluctuation (Note N7). Beyond the elastic range samples with dominant shear bands could be screened with neutron beam diffraction in an array of gauge volumes during halts of test stages, thereafter the pore system could be screened by X-ray attenuation. Such investigations could reveal how far fractal features and non-fractal trends can be reconciled by means of fractional derivatives (N2). Screening a belt with fractal uniformity for $\hat{\sigma}_3' > \hat{c}'$ as described in Sect. 5 could help clarify SWS, including the switch from $\hat{\epsilon}_\vartheta^e < \hat{\epsilon}_r^e < \hat{\epsilon}_1^e$ to $\hat{\epsilon}_r^e < \hat{\epsilon}_\vartheta^e < \hat{\epsilon}_1^e$ (shortening positive) with circumferential fluctuations. Investigations with dominant cracks (i.e., $\hat{\sigma}_3' < \hat{c}'$) could reveal features of rockburst.

7 Scaling up to lithosphere sections

The spatial and temporal fractality due to successive critical phenomena eludes a scaling up of lab findings by means of continuum models with simple materials. A complete analogy, i.e., equality of dimensionless ratios of all relevant quantities in model and prototype, cannot be achieved as initial and boundary conditions are less determined for lithosphere sections than for lab samples. Nevertheless analyses of lab and field observations reveal *scale-independent features*.

We consider first and mainly the range with *dominant shear bands*, i.e., with $\hat{\sigma}_3' > \hat{c}'$ quasi-locally. The Mohr–Coulomb condition (1) and the stress-dilatancy relation (2) can be generalized with invariants [11]. The implied principle of maximal dissipation ensues coaxiality of quasi-local stress and stretching rate tensors (assumed, e.g., for getting Fig. 5), and directions of shear bands can be related with quasi-local principal stress directions via tangents of stress circles. These properties, which require the symmetry $\hat{\sigma}_{ij}' = \hat{\sigma}_{ji}'$, cannot be strictly confirmed by field observations, but they are thus at least not refuted. Their scale-independence is also confirmed by observations with

micro-tectonic sandbox tests [21], and by the directional agreement of main faults by beach balls and from caving-in boreholes (Sect. 2).

This image is blurred by wild fluctuations and insufficiently known initial and boundary conditions of lithosphere sections. Differently to rock samples in multi-stage triaxial tests, the latter run through driven dilatation and spontaneous contraction in a wildly random succession [11], and the mineral composition is likewise less uniform. For instance, thus the directional agreement of faults in Fig. 1 and of horizontal shortening in Fig. 5 is imprecise, as is the agreement of shear band inclinations in Fig. 11 and fault inclinations in Fig. 2 (after shortening depths by factor 2). The seismicity in Lower Saxony indicates sparse chain reactions with a wildly random size distribution of uniformly aligned nearly collapsible lithosphere sections.

These findings could be of use also for other *deep-seated geotechnical operations* with $\hat{\sigma}_3' > \hat{c}'$ from about 1 km to 8 km depth skip [12]. The depletion-induced seismicity is bounded, but a technical triggering of natural earthquakes cannot generally be excluded as for our gas fields. Injections can induce a stronger seismicity if a wider and deeper range gets thus subcritical. The enhanced approach to collapsible states by an increase $\Delta\hat{p}_w$ of pore pressure can be estimated for lithosphere sections, but classical calculations of $\Delta\hat{p}_w$ and of seismic sources are questionable with fractality. The prevention of deeper-seated seismic events by many small injection-induced relaxing ones is out of reach as long as boreholes are scarcely deeper than about 8 km.

So how could deep-seated geotechnical operations get safer and more economical with the aid of *seismic monitoring*, especially with shear wave splitting (SWS)? Crampin and Peacock [1] point out that SWS is often used for improving the hydrocarbon production, and recommend it more generally for the stress-forecast of earthquakes. They argue that with an approach to collapsible states rock masses are uniformly aligned so that SWS gets observable despite fractal fluctuations. As shown in Note N6, SWS is justified with fractal fault patterns, not only with arrays of minute penny-shaped cracks as presumed by Crampin and Peacock [1]. SWS could indicate sizes of technically enhanced uniform alignment by dilatation prior to a seismogenic chain reaction of potentially dangerous size, especially during injections.

The task is more difficult for *rockbursts* in the range $\hat{\sigma}_3' < \hat{c}'$. Then the quasi-static driven overall dilatation with growing cracks in triaxial tests can no more be captured by a Mohr–Coulomb condition and a stress-dilatancy relation with quasi-local quantities. The subsequent collapse of the rock fabric is dilatant and tends to a disintegration. Such evolutions elude as yet mathematical treatment even with a

fractionally extended field theory. Caving-in of boreholes can still indicate overall directions of horizontal shortening despite $\hat{\sigma}_3' < \hat{c}'$ in the near-field (as, e.g., for Fig. 5), and hydraulic fracturing can indicate $\hat{\sigma}_3$. SWS observed in a glacier by Gajek et al. [6] speaks for fractally uniform zones with inter-connected cracks, these could also be achieved in triaxial tests. However, outbursts of injected fluids elude as yet numerical simulations and technical control. Fatal sudden motions of rock fragments along cavities and cliffs are as yet likewise not foreseeable. Nevertheless, a seismic monitoring could get more instructive for such cases by including SWS if this is better understood.

8 Conclusions and outlook

Comprehensive investigations, related with the depletion of gas fields in NW-Germany, reveal features of technically enhanced critical phenomena in the lithosphere which matter also for other geotechnical operations. Evolving faults and joints, or shear bands and cracks in rock samples, are tectonic or micro-tectonic dislocations, respectively, which elude Cauchy's concept of stress and strain. Differently from microscopic dislocations of metals, dislocations of rock can diverge in a wildly random way so that continuum models with methods of materials science fail. The tectonic drive cannot generally be represented by displacements or forces at boundaries of rather arbitrary lithosphere sections, and not by stresses as lithosphere sections are not loaded and cannot fail like technical structures. Fractal and non-fractal features can both be captured by means of quasi-local and -momentary quantities combined with fractional derivatives. Anyway, geological reconstructions of evolutions prior to depletion are indispensable.

Usually local collapsible states are characterized by a limit condition with a symmetric stress tensor, and seismicity is attributed to rapid shearing along faults. The Mohr–Coulomb limit condition is an approximation due to fluctuating relics of critical phenomena, this is confirmed by multi-stage triaxial tests with water-saturated sandstone samples. Such tests indicate two successive kinds of critical phenomena, namely slow driven ones with dilatation and fast spontaneous ones with contraction of the pore system. This order corresponds to successions of slow and fast tectonic dislocations in the lithosphere. Both modes can be reconstructed from observations in and around our gas fields, although they are blurred by overlying sediments and less known determining conditions than in lab tests. Dilating shear bands are inclined versus the vertical as obtained with Mohr–Coulomb tangents of effective stress

circles; this is observed at the surface of samples and nearly so with faults in seismic profiles.

Conventional attempts to explain the observed depletion-induced seismicity with an approach of estimated stresses to a Mohr–Coulomb limit prove to be insufficient. The employed smallest principal stress σ_3 by hydraulic fracturing is at best a crude estimate as the fractality is not taken into account. The usual combination of the reduction of such σ_3-values with a decrease of the pore water pressure p_w does not constitute a physical relationship. Actually rock masses are horizontally extended and vertically shortened near the rim and inside of gas inclusions, respectively, by their depletion as this leads to deepening troughs. Like with wider natural troughs this can lead sections of the lithosphere, which have about the same alignment as the overall tectonic extension, to collapsible states so that seismogenic chain reactions arise. Their onset is indicated by seismic sources near rims of gas inclusions, depicted by beach ball directions which match roughly the ones of major horizontal tectonic shortening. Corner frequencies and plateaus of seismic spectra indicate distances of main faults like widths of gas fields, and magnitudes of depletion-induced seismic events up to about 3, whereas a deeper-seated natural earthquake of about 4.3 occurred independently of the depletion.

Sandstone samples in multi-stage triaxial tests exhibit fractal patterns of shear bands if the minor quasi-local effective stress $\hat{\sigma}'_3$ exceeds the gradually dwindling cohesion $\hat{c}'$ (except near the endplates where $\hat{c}'$ dwindles less). For this range, the driven dilatation and stressing can be captured by a stress-dilatancy relation with an additional pressure for $\hat{c}'$. If the dilatation reaches a critical pore volume fraction, the rock fabric collapses with contraction so that the pore water pressure rises temporarily. This occurs in a seismogenic chain reaction with enhancement by seismic waves and diffusion of pore water. Similar successions of driven dilatation and spontaneous contraction occur in situ, though with a wildly random distribution of sizes, and can be enhanced by geotechnical operations.

Stresses cannot be observed in rock samples, but related elastic strains are indicated by changes of lattice plane distances which can be observed via the diffraction of neutron beams. Uniaxial tests with initially intact rock samples exhibit non-uniform changes of lattice plane distances which refute basic assumptions of continuum mechanics and materials science. A succession of micro-tectonic dislocations is indicated by means of novel triaxial tests in a setup for nine directions of diffracted neutron beams. Increases of overall stress and pore water pressure lead to wildly fluctuating changes of lattice plane distances. Further investigations of this kind could reveal how fabric stresses evolve alongside with shear band patterns in the

range $\hat{\sigma}'_3 > \hat{c}'$. The diffraction of neutron beams in uniaxial tests shows that for them cracks dominate, this holds also true in the range $0 < \hat{\sigma}'_3 < \hat{c}'$. The discrimination by means of $\hat{c}'$ and $\hat{\sigma}'_3$ is confirmed by X-ray tomographies with sandstone samples.

Successions of driven and spontaneous tectonic critical phenomena cannot be captured by mono-causal relations, and their fractality eludes present numerical models. Despite or just due to this indeterminacy states and mechanisms should and could be clarified with rock samples as analogue models because critical phenomena exhibit scale-independent features. Triaxial experiments should combine—simultaneously or with sets of equivalent rock samples—multi-stage boundary conditions with seismometry, X-ray tomography and/or diffraction of neutron beams. Thus, successions of driven and spontaneous critical phenomena could be observed in detail. A splitting of shear waves could also be observed in such multi-stage triaxial tests. Adequate state variables determining the sum of elastic and surface energies could be identified, especially for critical points and successions of them. This could help understand critical phenomena, also by comparison with observations at lithosphere sections.

Depletion-induced seismic events were harmless in NW-Germany, but the achieved better understanding could help keep critical phenomena small enough during other geotechnical operations. In particular, injections for harvesting thermal energy or solubles, for storing energy, or for sequestration of fluids, induce earthquakes. These could get too big in tectonically active zones, whereas small repeated injections could prevent the former by a gradual relaxation. Outbreaks of injected fluids via rockbursts elude as yet a sufficient control. The task is more difficult with rockbursts at cliffs or into cavities. However, the monitoring of split shear waves could indicate a uniform alignment by driven critical phenomena prior to an earthquake or outbreak of unacceptable size. All geotechnical operations imply successive critical phenomena, the fractality of which requires extended numerical models with fractional derivatives. Seismic and hydraulic monitoring are indispensable, and a better understanding of mechanisms can be achieved by means of sophisticated experiments.

Who contributed what

Except one of us (GG), we worked out a report on depletion-induced seismicity [24]. CL contributed triaxial tests, GG took over his findings for revising the principle of effective stress, both used them for clarifying tectonic mechanisms. CS and FS contributed experiments and analyses with neutron diffraction.

NOTES

N1: Cauchy proposed a symmetric matrix σ_{ij} of stress components as internal force densities, related with cubical volume elements of a continuous elastic solid. The latter may also imply inter-crystallite dislocations as long as fluctuation wavelengths are locally confined. This is no more the case with tectonic dislocations, therefore the usual combination of Cauchy stress components with a fault in a cube constitutes a contradiction in terms. One may nevertheless postulate an average force density $\hat{\sigma}'_{ij}$ with $\hat{\sigma}'_{ij} = \hat{\sigma}'_{ji}$ for inspection cubes with fractal uniformity, but except directions this quasi-local stress tensor depends on the cube size [11] and cannot capture polar effects. It can be reconciled with non-fractal trends by means of fractional gradients.

N2: The fractional derivative $d^{\alpha}f/dx^{\alpha}$ of a function $f(x)$ is the weighted average of difference quotients for sections of lengths $\Delta x = \xi d_r$ around a site x with the weighting factor $1/\xi^{\alpha}$, a reference length d_r and $0 < \alpha < 2$. Integration of $d^{\alpha}f/dx^{\alpha} = 0$ (i.e., uniformity) leads to $f \propto (x/d_r)^{\alpha}$, and extending to three dimensions the solid mass m in a cube grows thus with its width d by $m = m_r(d/d_r)^{3\alpha}$ with $m = m_r$ for $d = d_r$. With α just below 1 this characterizes fractally uniform rock as its pore volume fraction is slightly higher with wider faults. More generally, the fractional gradient ∇^{α}_{ij} of a quasi-local quantity $\hat{q}_i(x_j, t)$ tends to zero if d is in the range of fractal uniformity; this has a lower bound which can serve as d_r so that units of length do not matter. $d^{\beta}f/dt^{\beta}$ is defined analogously, its vanishing means fractal stationarity of a quasi-momentary quantity, and it requires a reference time t_r which equals d_r/v_d with a speed of drive v_d. The same exponent just below 1 for space and time, i.e., $\alpha = \beta$, is justified by the propagation of waves with tails of power spectra $v^2 \propto 1/f^{2\alpha}$ by means of a fractional wave equation [13].

N3 : In the standard execution and evaluation of hydraulic fracturing injection pressures for opening cracks around a vertical borehole, and for keeping them open, are converted into principal horizontal stresses by means of equations obtained with poro-elasticity, which are adapted by lab experiments with perforated intact rock samples [14]. The normal to a crack is assumed to have the direction of the smallest far-field principal stress σ_3. The previous water pressure in the near-field pore system and its fractality are not taken into account. Therefore, σ_3 by hydraulic fracturing can at best be a crude estimate of the quasi-local minimal principal stress $\hat{\sigma}_3$ near a borehole section, and observed directions of cracks can at best crudely indicate directions of $\hat{\sigma}_3$.

N4 : For inverting seismograms from different stations, as far as their correlations indicate a common seismic source (focus), the latter is usually substituted by a suddenly arising local force quadrupole instead of a stress drop [19]. A beach ball, representing a focal mechanism, is a graphical means to show the type of slip that occurs during an earthquake. Its projection shows the fault orientation and the slip on the lower half of a sphere surrounding the source. Seismic waves yield a pattern with four quadrants; in two of them the first motion at the seismometer is compressional (push), in the other two it is extensional (pull). The quadrants are separated by two great circles which represent nodal planes, viz. a fault plane and an auxiliary plane for relative displacements. Additional information from aftershocks can help identify a fault plane. This is a drastic simplification as seismic sources generating P-and S-waves evolve in a chain reaction, and also as propagating waves are dispersed in a fractal solid.

N5 : Plots of σ_3 versus p_w are called stress paths in reservoir engineering, and a 'stress path coefficient' $\Delta p_w / \Delta \sigma_3$ is assumed to characterize a gas field [25]. A plot of σ'_1 versus σ'_3 would be an effective stress path which could show rock properties, but a plot of σ_3 versus p_w cannot as it is not a solid stress path and as thus the principle of effective stress is ignored. An empirically nearly constant $\Delta p_w / \Delta \sigma_3$ is accidental, the more so as measured σ_3 and p_w are crude estimates. Such an approach of collapsible states in the middle of gas fields by their depletion is also misleading as there both $\hat{\sigma}'_1$ and $\hat{\sigma}'_3$ increase and $\hat{\sigma}'_1/\hat{\sigma}'_3$ decreases with the laterally confined vertical shortening.

N6 : Terzaghi took over Fourier's equation of heat conduction with the pore water pressure p_w instead of the temperature T for a water-saturated elastic porous solid. He spoke of the dissipation of pore pressure during a consolidation, although only extensive quantities (e.g., heat or pore water) can be dispersed. Biot took the implied volume change of pore water with an arbitrary reference as a state variable. Avoiding this error, Terzaghi's principle of effective stress can be derived from the neutrality of the mineral with regard to changes of p_w [12].

N7 : The quasi-local specific elastic energy $\hat{w}_e$ is the potential of the quasi-local effective stress by $\hat{\sigma}'_{ij} = (1 - \mu)\partial \hat{w}_e / \partial \hat{\epsilon}^e_{ij}$ with the quasi-local elastic strain tensor $\hat{\epsilon}^e_{ij}$ [11]. Therein the factor $1 - \mu \approx 0.2$ means that about 4/5 of the elastic energy does not contribute to the force transfer due to spatial fluctuations from critical phenomena. μ is slightly smaller off critical points, but cannot vanish by reversals as with sand by densification. The balance of linear momentum in an elastic range (widened by cohesion) can be expressed by a fractional wave equation [13]. Therein the matrix of differential stiffness is given by the second-order derivatives of $\hat{w}_e(\hat{\epsilon}^e_{ij})$, which means a stress-aligned orthogonal anisotropy. Fourier and Laplace

transformations of the fractional wave equation combined with a plane Dirac pulse lead to shear wave splitting (SWS) by means of an eigenvalue problem [11]. This requires symmetry $\hat{\epsilon}_{ij}^e = \hat{\epsilon}_{ji}^e$ and spatio-temporal iso-fractality. Without fractality, SWS is obtained as for an anisotropic solid with $\alpha = \beta = 1$.

N8 : A symmetric elastic deformation tensor ϵ_{ij}^e implies a stretching $\epsilon_k^e = \epsilon_{ij}^e e_i^k e_j^k$ in the direction with unit vector e_i^k, so the six components of ϵ_{ij}^e can be calculated from six changes of lattice plane distances in six directions. This inversion can fail with shearing for which certain grid plane distances do not change. Neutron beams are diffusely diffracted by a random composite of crystallites, but peak shifts of neutron counts versus times of flight can still yield an average strain tensor $\bar{\epsilon}_{ij}^e$ of a crystallite composite in a gauge volume via average strains $\bar{e}_i^e$. However, due to the fractal pore system of rock with cracks and shear bands its average elastic strain $\hat{\epsilon}_{ij}^e$ in a gauge volume has a bigger deviatoric and a much bigger volumetric part than $\bar{\epsilon}_{ij}^e$. Both dwindle with the size of the gauge volume in case of fractal uniformity.

N9 : Spatial fluctuations are the same for stress and elastic strain and have a scale-independent coefficient of variation for a quasi-local fractality, which is proportional to the reduction parameter μ (N7). The relation of $\hat{\sigma}_{ij}'$ with $\hat{\epsilon}_{ij}^e$ via $\hat{w}_e$ means that presumed symmetries $\hat{\sigma}_{ij}' = \hat{\sigma}_{ji}'$ and $\hat{\epsilon}_{ij}^e = \hat{\epsilon}_{ji}^e$ are equivalent. This symmetry is necessary for getting principal components and axial directions, coaxiality of stress and stretching rate tensors, and a splitting of shear waves [11]. Assuming coaxiality and equal Lode parameters of the elastic strain tensors $\bar{\epsilon}_{ij}^e$ and $\hat{\epsilon}_{ij}^e$ of crystallites and porous fabric, respectively, the relation of both tensors is determined by the equality of the related elastic energies except the factor $1 - \mu$. Beyond the empirical relation of crystallite and fabric strains from uniaxial tests [4], un- an reloading in the elastic range enables validation and calibration.

References

1. Crampin S, Peacock S (2008) A review of the current understanding of the seismic shear wave splitting in the Earth's crust and common fallacies in understanding. Sci Direct, Wave Motion 45:675–722
2. Desrues J, Andò E, Mevoli Ando FA, Debove L, Viggiani G (2019) How does strain localise in standard triaxial tests on sand: Revisiting the mechanism 20 years on 2019. Mech Res Comm 92:142–146
3. Fonseca J, Besuelle P, Viggiani G (2013) Micromechanisms of inelastic deformations in sandstones: an insight using X-ray tomography. Geotech Lett 3(2):78–83
4. Frischbutter F, Neov D, Scheffzük Ch, Vrana M, Walther K (2000) Lattice strain measurements on sandstones under load using neutron diffraction. J Struct Geol 22:1587–1600
5. Frischbutter A, Janssen Ch, Scheffzük Ch, Walther K, Ullemeyer K, Behrmann JH, Nikitin AN, Ivankina TI, Kern H, Leiss B (2006) Strain and Texture Measurements on Geological Samples Using Neutron Diffraction at IBR-2, Joint Institute for Nuclear Research, Dubna (Russia). Physics of Particles and Nuclei, Vol. 37, Suppl. 1, pp. S45–S68,
6. Gajek W, Gräff D, Hellmann S, Alan W, Rempel AW, Walter F (2021) Diurnal expansion and contraction of englacial fracture networks revealed by seismic shear wave splitting. Commun Earth Environ 2(1):1–8
7. Gast R (1988) Rifting im Rotliegenden Niedersachsens. *Die Geowissenschaften*, Alfred-Wegener-Stiftung, Heft 4
8. Gast R, Gundlach T (2006) Permian strike-slip and extensional tectonics in Lower Saxony, Germany. Zeitschr Dtsch Ges Geowiss 157(1):41–56
9. Grasso JR, Wittlinger G (1990) Ten years of seismic monitoring over a gas field. Bull Seismol Soc Am 80(2):450–473
10. Griffiths L, Dautria J, Rodriguez J, Vera IA, Iranpour K, Sauvin G, Park J, Sarout J, Soldal M, Grande L, Oye V, Dewhurst D, Mondol MD, Choi JC (2019) Inferring microseismic source mechanisms and in situ stresses during triaxial deformation of a North-Sea-analogue sandstone. Adv Geosc 49:85–93
11. Gudehus G, Lempp C (2022) Tectonic critical phenomena with dilatancy in analogue models (Part 1) and lithosphere sections (2). Hallesch Jahrb Geowiss 45
12. Gudehus G (2021) Implications of the principle of effective stress. Acta Geotech 16(6):1939–1947
13. Gudehus G, Touplikiotis A (2016) Wave propagation with energy diffusion in a fractal solid and its fractional image. Soil Dyn Earthq Eng 89:38–48
14. Haimson BC (1978) The Hydrofracturing Stress Measuring Method and Recent Field Results. Int J Rock Mech Min Sci Geomech Abstr 15:167–178
15. Heidbach O, Rajabi M, Cui X, Fuchs K, Miller B, Reinecker J, Reiter K, Tingay M, Wenzel F, Xie F, Ziegler MO, Zoback M-L, Zoback MD (2018) The World Stress Map database release 2016: Crustal stress pattern across scales. Tectonophysics 744:484–498. https://doi.org/10.1016/j.tecto
16. Leary PC (1997) Rock as a critical-point system and the inherent implausibility of reliable earthquake prediction. Geophys J Int 131:451–466
17. Lempp C, Lerche I (2006) Correlation of stress directions across the North German Basin: suprasalt and subsalt differences. Zeitschrift der Deutschen Gesellschaft für Geowissenschaften 279–297

18. Lempp C, Menezes F, Schöner A (2020) Evolution of shear bands and cracks in multi-stage triaxial tests with water-saturated sandstone: a study of micro-tectonics with a fractal perspective. J Struct Geol 138:104092

19. Madariaga R (2007) Seismic source theory. Treatise Geophys 4:59–82

20. Mandelbrot B (1999) Multifractals and 1/f-noise - wild self-affinity in physics. Springer, New York

21. Mandl G (1988) Mechanics of tectonic faulting, models and basic concepts. Elsevier, Amsterdam

22. Menezes F (2022) Stress-dilatancy behavior of saturated sandstone samples in triaxial tests. Paper for Act Geot

23. Müller BI, Schilling FR, Röckel T, Heidbach O (2018) Induced seismicity in reservoirs: stress makes the difference. Erdöl Erdgas Kohle 1:33–37

24. Müller BI, Scheffzük C, Schilling FR, Westerhaus M, Zippelt K, Wampach M, Röckel T, Lempp C, Schöner A (2020) Reservoir-Management and Seismicity - Strategies to reduce induced seismicity. DGMK Res. Proj. 776, Final Report

25. Nelson EJ, Hillis RR, Meyer JJ, Mildren SD, Van Nispen D, Briner A (2005) The reservoir stress path and its implications for water-flooding, Champion Southeast field, Brunei. Amer Rock Mech Ass USRMS, 05-775, 2005

26. Polsky Y, Dessieux L, An K, Anovitz LM, Bingham P, Carmichael J (2013) Development of a neutron diffraction based experimental capability for investigating hydraulic fracturing for EGS-like conditions. Proc 38th Worksh Geoth Res Eng, Stanford University

27. Röckel T, Lempp C (2003) Der Spannungszustand im Norddeutschen Becken. Erdöl Erdgas Kohle 119/2

28. Rowe PW (1962) The stress-dilatancy relation for static equilibrium of an assembly of particles in contact. Proc Royal Soc London Ser A Math Phys Sci 269(1339):500–527

29. Scheffzük Ch, Zang A, Stephansson O, Ullemeyer K, Schilling FR (2015) Applied residual strain and texture investigations by means of neutron time-of-flight diffraction combined with acoustic emission detection: Application to a gneiss sample from Forsmark, Sweden. IOP Conf Series: Mat Sci Eng 82:012071

30. Terzaghi K (1936) The shearing resistance of saturated soils and the angle between the planes of shear. Proc 1st Int Conf Soil Mech Found Eng, D-7

31. Uta P (2017) Recent intraplate earthquakes in Northwest Germany - Glacial isostatic adjustment and/or a consequence of hydrocarbon production? Ph.D. thesis Univ. Hannover, free online

32. Uta P, Brandes C, Gestermann N, Plenefisch T, Kaiser D, Bönnemann C, Winsemann J (2018) The Re-evaluation of the 2004 Rotenburg MW 4.4 Earthquake. Geophys Res Abstr 20, EGU2018-10627-1

33. Van Eck T, Goutbeek F, Haak H, Dost B (2006) Seismic hazard due to small-magnitude, shallow-source, induced earthquakes in The Netherlands. Eng Geol 87:105–121

34. Vrolijk PJ, Urai J, Kettermann M (2016) Clay smear: Review of mechanisms and applications. J Struct Geol 86:95–152